Hot Deformation and Dynamic Recrystallization of 18%Mn Twinning-Induced Plasticity Steels

Vladimir Torganchuk,* Olga Rybalchenko, Sergey Vladimirovich Dobatkin, Andrey Belyakov, and Rustam Kaibyshev

The deformation behavior of 18%Mn twinning-induced plasticity (TWIP) steels with 0.4%C or 0.6%C is studied by means of isothermal compression tests in the temperature range of 973–1373 K at the strain rates of 10^{-3}–10^{-1} s^{-1}. The hot working is accompanied by the development of discontinuous dynamic recrystallization (DRX), which is commonly advanced by an increase in deformation temperature and/or a decrease in strain rate. A decrease in the carbon content promotes the DRX development, though the flow stresses scarcely depend on the carbon content. The change in the DRX kinetics results in the specific distributions of the grain orientation spread (GOS) among the DRX grains, depending on deformation conditions. The maximal fraction of grains with small GOS below 1° corresponding to rapid DRX development is observed at certain temperature/ strain rate, although the DRX fraction increases with a decrease in temperature-compensated strain rate and can be related to the fraction of grains with GOS below 4°. The texture of DRX grains is also determined by the orientations of grains with GOS below 4°. The grain boundary mobility for the DRX grain growth is characterized by an activation energy close to that for grain boundary diffusion.

1. Introduction

A decrease in the car weight leads to a reduction in harmful emissions. It is believed that every 10% in reducing the weight can reduce fuel consumption by 5%.[1] On the other hand, an overall level of safety requires strong, weighty constructions. Therefore, advanced high strength steels should be developed to follow the current trends in the fields of environmental safety and automobile reliability. The development of new steels coupled with their

processing methods can produce cars that meet the requirements of the safety of passengers. These steels should possess high strength properties and be reliable at relatively low cost.[2,3] According to forecast for the past ten years until 2020, the share of high-strength steels for automotive applications should increase more than fourfold.[4]

High-Mn twinning-induced plasticity (TWIP) steels are ones of the most promising representatives of the new steel generation. The TWIP steels have aroused a great interest in automobile industry due to their outstanding plasticity combined with rather high ultimate tensile strength. Such steels are characterized by a high strain-hardening rate owing to deformation twinning.[5] The twinning in such steels occurs at stacking fault energy (SFE) of ≈15–45 mJ m^{-2}. The high strength and plasticity of TWIP steels result from decreasing the mean free path of a dislocation caused by progressive development of twin boundaries leading to substantial grain subdivision down to nanocrystallites.[6] Thus, the twinning-assisted increase in the dislocation density results in the strain hardening, which suppresses the strain localization and necking. A common disadvantage of high-Mn TWIP steels is their relatively low yield strength, which comprises ≈200 MPa in coarse-grained annealed conditions, although grain refinement can remarkably strengthen the steel.[6] A decrease in the mean grain size below 2 μm has resulted in the yield strength above 500 MPa along with TWIP effect in a high-Mn steel.[7] The strength of TWIP steels has been frequently discussed in terms of modified Hall–Petch relationship including the dislocation strengthening.[8,9] The latter increases both the yield strength and ultimate tensile strength, though plasticity may substantially degrade.[5] A beneficial combination of strength and plasticity, therefore, can be obtained owing to appropriate microstructure with desired grain size and dislocation density.

Commonly, the semiproducts of high-Mn TWIP steels are processed by thermomechanical treatment involving hot working. Hot deformation of high-Mn austenitic TWIP steels with low SFE is accompanied by the development of discontinuous dynamic recrystallization (DRX), which may lead to the microstructures with desired grain size and dislocation density, providing required level of mechanical properties.[10–13] Discontinuous DRX develops through nucleation and growth of new grains consuming work-hardened neighbors with high

V. Torganchuk, Dr. A. Belyakov, Dr. R. Kaibyshev
Laboratory of Mechanical Properties of Nanostructured Materials and Superalloys
Belgorod State University
Pobeda 85, Belgorod 308015, Russia
E-mail: torganchuk@bsu.edu.ru

Dr. O. Rybalchenko, Dr. S. V. Dobatkin
Laboratory of Light and Non-Ferrous Metals
A. A. Baikov Institute of Metallurgy and Materials Science of RAS
Leninsky prospect 49, Moscow 119334, Russia

Dr. O. Rybalchenko, Dr. S. V. Dobatkin
Laboratory of Hybrid Nanostructured Materials
National University of Science and Technology "MISIS"
Leninsky prospect 4, Moscow 119991, Russia

The ORCID identification number(s) for the author(s) of this article can be found under https://doi.org/10.1002/adem.202000098.

ADVANCED
SCIENCE NEWS
www.advancedsciencenews.com

ADVANCED
ENGINEERING
MATERIALS
www.aem-journal.com

dislocation density, which is a driving force for the DRX development.[14] Hence, hot deformation of austenitic steels is commonly accompanied by an increase in the flow stress to a maximum (peak stress) followed by strain softening, which indicates the DRX development as confirmed by microstructural observations.[15,16] Discontinuous DRX is essentially a cyclic process,[14] when the new grains nucleate, grow, and work-harden repeatedly during deformation, resulting in the DRX microstructure with various dislocation densities. The presence of dislocation substructures has been considered as an additional strengthener in a high-Mn steel with the DRX microstructure, providing beneficial combination of mechanical properties.[17] However, effect of processing conditions on the dislocation density and its distribution in DRX microstructures is still unclear. The deformation and DRX mechanisms are very important for the selection of appropriate processing regimes to obtain a favorable combination of microstructure and mechanical properties.
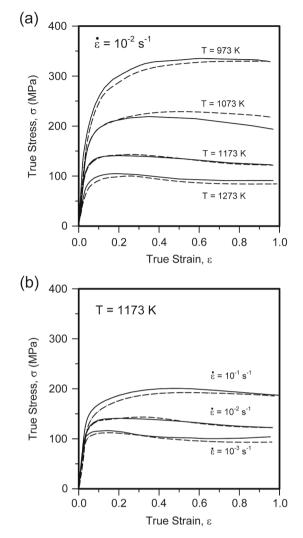
The aim of this study is to clarify the hot deformation behavior of promising 18%Mn TWIP steels, which may exhibit a tensile elongation above 60% with a strength of more than 1000 MPa.[18] The study is particularly focused on the relationship between the DRX mechanisms and dislocation substructures upon hot working of steels with different contents of carbon, which is one of the main alloying elements of high-Mn TWIP steels, that strongly affects the mechanical properties.[8,10,17–21] The deep understanding the mechanisms of microstructure evolution during hot working of structural steels and alloys is very important for the development of intelligent processing technologies providing semiproducts with controlled mechanical properties.

2. Results

2.1. Deformation Behavior

The true stress–strain curves of the Fe–0.4C–18Mn and Fe–0.6C–18Mn TWIP steels as obtained at various temperatures and strain rates are shown in **Figure 1**. The flow curves are commonly characterized by several specific portions. Namely, following strain hardening at early deformation, the flow stress approaches a maximum followed by strain softening. A steady-state deformation behavior occurs at sufficiently large strain as promoted by an increase in temperature and/or a decrease in strain rate. Such deformation behavior with a flow stress maximum followed by strain softening suggests the development of discontinuous DRX.[15,22–24] The strain corresponding to the peak stress decreases with a decrease in strain rate ($\dot{\varepsilon}$) and/or an increase in deformation temperature (T), indicating an acceleration of DRX with a decrease in temperature-compensated strain rate (Zener–Hollomon parameter, $Z = \dot{\varepsilon} \exp(Q/RT)$, where Q is the activation energy and R is the universal gas constant).[25,26] Variation in the carbon content does not lead to any significant change in the stress–strain curves within the studied range of temperatures and strain rates. The stress–strain curves for the Fe–0.4C–18Mn and Fe–0.6C–18Mn steel samples, which are compressed at the same conditions, are almost the same, although characteristic flow stages, e.g., the peak stress, occur at smaller strains in the samples with lower carbon content. This may indicate somewhat faster DRX kinetics in the steel with lower carbon content.

Figure 1. Typical true stress–strain curves for Fe–0.4C–18Mn (solid lines) and Fe–0.6C–18Mn (dashed lines) steel samples subjected to compression a) at $\dot{\varepsilon} = 10^{-2}\,\mathrm{s}^{-1}$ and $973 \leq T \leq 1273$ K and b) at $T = 1173$ K and at $10^{-3}\,\mathrm{s}^{-1} \leq \dot{\varepsilon} \leq 10^{-1}\,\mathrm{s}^{-1}$.

The relationship between the flow stress (σ) and temperature/strain rate can be expressed as follows[27,28]

$$\dot{\varepsilon} = A \left(\frac{\sigma}{G} \right)^n \exp\left(\frac{-Q}{RT} \right) \tag{1}$$

$$\dot{\varepsilon} = A_1 \exp\left(\beta \frac{\sigma}{G} \right) \exp\left(\frac{-Q}{RT} \right) \tag{2}$$

$$\dot{\varepsilon} = A_2 \left(\sinh\left(\alpha \frac{\sigma}{G} \right) \right)^{n_2} \exp\left(\frac{-Q}{RT} \right) \tag{3}$$

where A, A_1, A_2, n, β, $\alpha \approx \beta/n$, and n_2 are fitting parameters, which can be related to material properties in the framework of respective theoretical models,[27] and G is the shear modulus. Equation (1) is frequently used for hot deformation at relatively low flow stress, whereas Equation (2) is valid for a high stress domain of hot working, where the power law breaks down.

Equation (3) combines both Equation (1) and (2); i.e., it transforms to power law at low stresses or becomes exponential function at high stresses and can be used in a wide range of warm- to hot-working conditions. Considering the temperature dependence of the shear modulus,[27] the experimental data for the peak flow stress are plotted in **Figure 2** according to Equation (1)–(3), leading to the deformation activation energy of $263\,\text{kJ}\,\text{mol}^{-1}$. It should be noted in Figure 2 that both Fe–0.4C–18Mn and Fe–0.6C–18Mn steels are characterized by the same dependencies irrespective of different carbon contents. Obtained value of activation energy is close to that of volume diffusion[27] and smaller than those reported in other studies on austenitic steels.[28] The difference in the calculated activation energy is associated with the temperature dependence of the shear modulus. Neglecting of the latter results in overestimation of the energy values.[29]

The effect of deformation conditions on the peak flow stress (σ_p) is shown in **Figure 3**. It is clearly seen that σ_p can be expressed by a power law function of Z with an exponent of 1/6 in the range of $Z < 10^{13}\,\text{s}^{-1}$. Similar deformation behaviors with exponents of 1/4 to 1/5 have been reported for other austenitic steels compressed under hot-working conditions, when the flow stress sensitively depends on temperature and/or strain rate.[30] An increase in Z above $13^{13}\,\text{s}^{-1}$ is accompanied by a drastic decrease in the exponent that
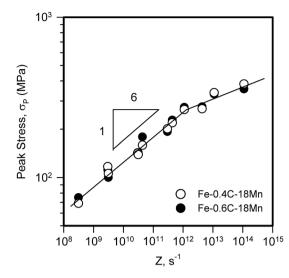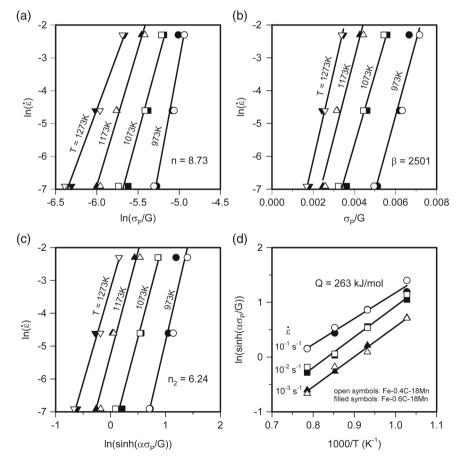

Figure 3. Relationship between the peak flow stress and temperature-compensated strain rate (Z) for hot compression of Fe–0.4C–18Mn and Fe–0.6C–18Mn steel samples.

corresponds to transition from thermal to athermal deformation behavior with a weak temperature/strain rate dependence of the flow stress.

Figure 2. Relationships between a) $\ln\dot{\varepsilon}$ and $\ln(\sigma_P/G)$, b) $\ln\dot{\varepsilon}$ and σ_P/G, c) $\ln\dot{\varepsilon}$ and $\ln(\sinh(\alpha\sigma_P/G))$, and d) $\ln(\sinh(\alpha\sigma_P/G))$ and $1/T$ for hot compression of Fe–0.4C–18Mn and Fe–0.6C–18Mn steel samples.

**ADVANCED
SCIENCE NEWS**

www.advancedsciencenews.com

**ADVANCED
ENGINEERING
MATERIALS**

www.aem-journal.com
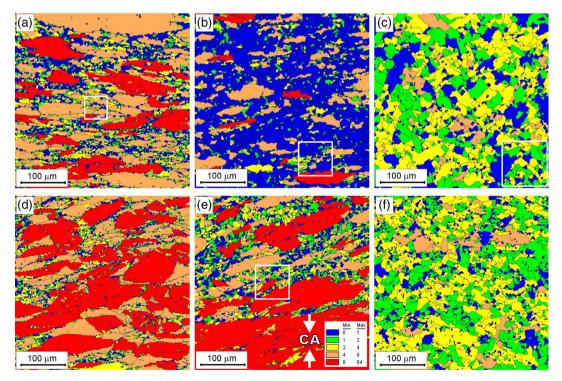
2.2. Deformation Microstructures

Typical microstructures that develop in the Fe–0.4C–18Mn and Fe–0.6C–18Mn steel samples during isothermal compressions at different temperatures and strain rates corresponding to high, medium, and low Z are shown in **Figure 4** as grain orientation spread (GOS) mappings. The developed microstructures significantly depend on the deformation temperature. The pan-caked original grains are observed in the both steels after compressions at relatively low temperatures, e.g., 973 K in Figure 4a,d. Numerous fine grains are clearly seen in these figures along the boundaries of highly flattened original grains. These are typical necklace DRX microstructures resulted from rapid development of new fine DRX grains by bulging of frequently serrated boundaries.[31] An increase in the deformation temperature promotes the DRX development. Entirely DRX microstructures that were developed during compressions at 1173 K are shown in Figure 4c,f. Note, here, that the experimental conditions have been selected to minimize the effect of post-dynamic recrystallization (post-DRX) on the developed microstructures. Therefore, the effect of post-DRX on the deformation microstructures is neglected.

In general, the discontinuous DRX microstructures consist of DRX nuclei, growing DRX grains, and work-hardened grains awaiting the next DRX nucleation.[32] Such microstructures result from cyclic DRX development, including sequential nucleation, growth, work-hardening of DRX grains, and, then, again nucleation Note, here, that the DRX grain size distribution remains invariant during the steady-state deformation because of concurrent shrinkage and growth of DRX grains.[33] The DRX grains corresponding to different DRX stages should be differentiated by the GOS values. Namely, DRX nuclei should have small GOS, whereas growing DRX grains and work-hardened DRX grains should be characterized by medium GOS and relatively large GOS, respectively. Indeed, the fraction of grains with GOS below 1° corresponding to just developed DRX grains substantially increases in the Fe–0.4C–18Mn steel samples with an increase in deformation temperature from 973 to 1073 K (see Figure 4a,b). It is interesting that a further increase in temperature to 1173 K (Figure 4c) is accompanied by a decrease in the fraction of grains with small GOS below 1°. Such changes should be considered as typical of discontinuous DRX, when overlapping of DRX cycles results in specific distribution of grains corresponding to different DRX stages. It should be noted that the both steels demonstrate similar DRX behavior, although Fe–0.6C–18Mn steel is characterized by remarkably smaller fraction of low GOS grains, especially at relatively low temperatures (see Figure 4b,e), that testifies to lower DRX kinetics in the steel with larger carbon content.

The different DRX kinetics in the present steel samples result in distinctive distribution of grains with various GOS (**Figure 5** and **6**). The necklace DRX microstructures evolved at a relatively low temperature of 973 K are characterized by the large fractions of grains with GOS above 4°. An increase in deformation temperature promotes the DRX development. Therefore, the fraction of grains with large GOS corresponding to unrecrystallized remnants decreases, whereas the fraction of grains with small GOS increases. The large fraction above 0.6

Figure 4. GOS in deformation microstructures of a–c) Fe–0.4C–18Mn and d–f) Fe–0.6C–18Mn steel samples subjected to compression at a,d) $T = 973$ K and $\dot{\varepsilon} = 10^{-2}\,s^{-1}$, b,e) $T = 1073$ K and $\dot{\varepsilon} = 10^{-2}\,s^{-1}$, and c,f) $T = 1173$ K and $\dot{\varepsilon} = 10^{-3}\,s^{-1}$. High-angle grain boundaries are indicated by the black lines. The arrows indicate the CA direction. Selected portions are represented in Figure 12.
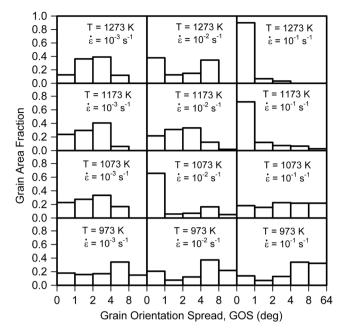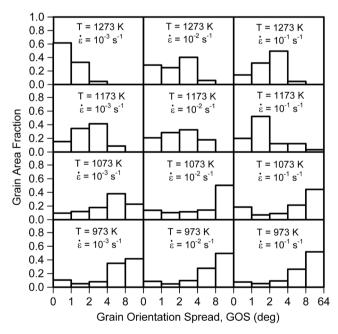
2000098 (4 of 11)

Figure 5. Distributions of GOS in the Fe–0.4C–18Mn steel samples subjected to hot compression at indicated conditions.

Figure 6. Distributions of GOS in the Fe–0.6C–18Mn steel samples subjected to hot compression at indicated conditions.
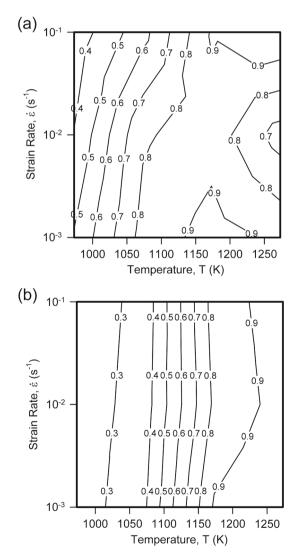
when DRX is almost completed. The similar GOS distributions are observed in the Fe–0.6C–18Mn steel samples after compressions at $T \geq 1173\,K$ and $\dot{\varepsilon} \leq 10^{-1}\,s^{-1}$. It should be noted that small fractions of grains with large GOS above 4° are observed in the uniform DRX microstructures irrespective of deformation conditions at least in the studied range of temperatures and strain rates. Therefore, the DRX microstructures may contain a certain amount of work-hardened grains with the mean deviation from average orientation up to 8°. The fractions of such grains with GOS above (or below) 4° should also reflect the DRX kinetics.

Under constant strain rate, the DRX kinetics can be evaluated by the DRX fraction, i.e., the fraction of grains with GOS below some critical value, that developed in the specimens compressed to the same strain, which is in direct proportion to deformation time. The fractions of grains with GOS below 4° are plotted for various temperatures and strain rates in **Figure 7** to consider the DRX kinetics. Note, here, that increasing the fractions of these
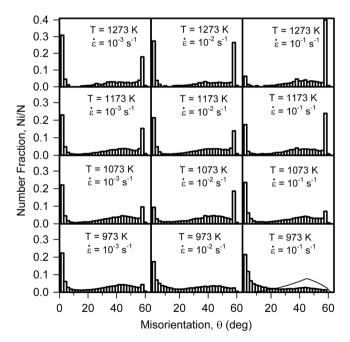

Figure 7. Dependence of grain area fraction with GOS below 4° in the a) Fe–0.4C–18Mn and b) Fe–0.6C–18Mn steel samples on deformation temperature and strain rate.

of DRX grains with small GOS below 1° appears in the Fe–0.4C–18Mn steel samples after deformation at $\dot{\varepsilon} = 10^{-2}\,s^{-1}$ and $T = 1073\,K$ or at $\dot{\varepsilon} = 10^{-1}\,s^{-1}$ and $T \geq 1173\,K$, whereas that in the Fe–0.6C–18Mn steel samples is observed at $\dot{\varepsilon} = 10^{-3}\,s^{-1}$ and $T = 1273\,K$. The fractions of grains with large GOS above 4° in the Fe–0.4C–18Mn steel samples are quite small after compressions to a strain of 1.0 at $T \geq 1073\,K$ and $\dot{\varepsilon} \leq 10^{-2}\,s^{-1}$,

grains with an increase in deformation temperature and/or a decrease in strain rate roughly corresponds to the DRX fractions. On the other hand, a decrease in the fraction of these small GOS grains at high temperatures indicates a relative slowing down of the DRX kinetics rather than a decrease in the DRX fraction. It is clearly seen in Figure 7a that DRX readily develops in the Fe–0.4C–18Mn steel samples. The same fractions in the range of 0.3–0.8 of the grains with GOS below 4° can be obtained in the Fe–0.4C–18Mn steel samples at temperatures about 50–100 K below those for the Fe–0.6C–18Mn steel samples. For instance, the fraction of grains with small GOS below 4° in the Fe–0.4C–18Mn steel samples attains 0.8 in the range of 1050–1150 K depending on strain rate. In contrast, the same fraction of grains with small GOS below 4° in the Fe–0.6C–18Mn steel samples can be achieved at temperatures above 1150 K, and it scarcely depends on strain rate (Figure 7b). Therefore, it can be concluded that steel with lower carbon content exhibits much faster DRX kinetics, which, in turn, suggests faster growth of DRX grains.
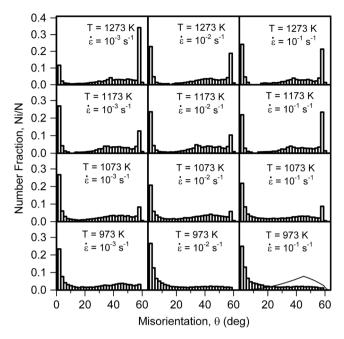
The DRX development affects significantly the grain boundary misorientation distributions (**Figure 8** and **9**). Commonly, the developed misorientation distributions can be characterized by two distinctive components. Those are sharp peaks against small misorientations below 10° and large misorientations of 60°. The former represents low-angle dislocation subboundaries, which evolve in work-hardened grains, and the latter corresponds to annealing twins that frequently develop in growing DRX grains.[34,35] The rest of misorientations between these two peaks appears with relatively small fractions and looks like random misorientation distribution (the latter is indicated by solid line in Figure 8 and 9). Namely, their fraction gradually increases as misorientation increases to 45° and then decreases with a

Figure 9. Grain/subgrain boundary misorientation distributions for the Fe–0.6C–18Mn steel samples subjected to hot compressions under indicated conditions.

further increase in misorientation. The relative fractions of low-angle subboundaries and 60° boundaries correlate with DRX extent. The large fractions of low-angle subboundaries are clearly seen in the samples compressed at a relatively low temperature of 973 K, whereas the fractions of twin boundaries are negligibly small in these necklace microstructures with small DRX fractions. The DRX development with an increase in temperature promotes the annealing twin formation, leading to an increase in the fraction of 60° misorientations. It is worth noting that relatively large fractions of twin boundaries that exceed small fractions of low-angle subboundaries in Figure 8 and 9 appear in the DRX microstructures with large fractions of grains with small GOS below 1° in Figure 5 and 6. Another interesting feature of fully developed DRX microstructures is a rather large fraction of low-angle subboundaries. Almost the same fractions of low-angle subboundaries and twin boundaries indicate the dynamic equilibrium between the fractions of work-hardened grains and growing grains in the present DRX microstructures. Similar to GOS in Figure 5 and 6, the misorientation distributions in Figure 8 and 9 suggest faster DRX development in the steel samples with lower carbon content.

2.3. DRX Grains

In general, a decrease in deformation temperature and/or an increase in the strain rate result in a decrease in the DRX grain size.[22–24] The relationship between the DRX grains size and temperature-compensated strain rate is shown in **Figure 10**. The present DRX grain size was evaluated in the portions of microstructure with GOS below 4°. The DRX data for other austenitic steels[36–38] are also shown in Figure 10 for reference.
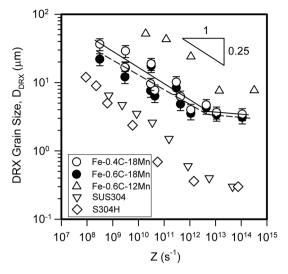

Figure 8. Grain/subgrain boundary misorientation distributions for the Fe–0.4C–18Mn steel samples subjected to hot compressions under indicated conditions.

Figure 10. Relationship between the DRX grain size and temperature-compensated strain rate (Z) for the present Fe–0.4C–18Mn and Fe–0.6C–18Mn steels, and other austenitic steels.[36–38]

The present DRX grain size can be expressed by a power law function of Z with an exponent of -0.25 in the range of $Z < 13^{13}\,\text{s}^{-1}$ corresponding to hot-working conditions. Almost the same results with the exponents of -0.3 to 0.4 were reported in other studies on DRX in austenite.[37–39] The change in the strong temperature/strain rate dependence of the DRX grain size to much weaker one at $Z > 10^{13}\,\text{s}^{-1}$ in Figure 10 clearly corresponds to similar change in the temperature/strain rate dependence of the peak flow stress in Figure 3, suggesting the transition from hot-working to warm-working conditions.
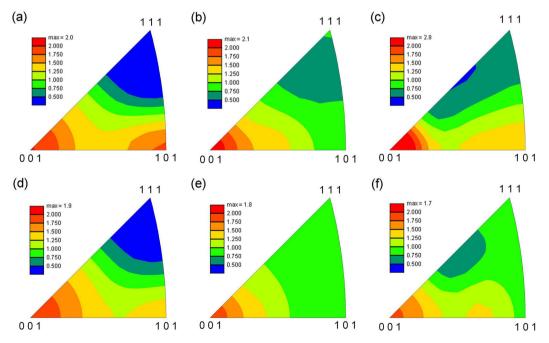
It is clearly seen in Figure 10 that the DRX grain size that evolved in various austenitic steels under the same deformation conditions significantly depends on the alloying extent. Namely, an increase in the alloying content of substitutes refines the DRX microstructure substantially. On the other hand, carbon has much weaker effect on the DRX grain size, although the present results suggest a remarkable decrease in the DRX grain size with an increase in carbon content. Such carbon effect on the DRX grain size may be associated with an increase in the drag pressure on the boundaries of growing DRX grains as the carbon content increases.

Typical orientations of DRX grains are illustrated by inverse pole figures (IPFs) for the compression axis (CA) in **Figure 11**. Note, here, that IPFs are shown for grains with GOS below 4°. All IPFs in Figure 11 are characterized by a small maximum around <001>. This is a typical feature of face centered cubic (fcc) metals/alloys subjected to discontinuous static recrystallization, when the recrystallized growing grains are mainly oriented with <001> along the normal direction.[40,41] IPFs of single <001> peak type are clearly seen in Figure 11b,e. Similar IPFs have been observed in a DRX austenitic steel after large hot strains.[42] IPFs in Figure 11b,e correspond to the samples with large fraction (above 0.8) of DRX grains with GOS below 4°, although the fractions of just developed DRX grains with GOS below 1° in these samples are quite different (see Figure 5 and 6). Almost the same similarity can be observed in Figure 11c,f. Therefore, it can be concluded that the DRX texture depends on the fraction of DRX grains with GOS below 4° irrespective of any differences in the DRX rate, which can be roughly related to the faction of DRX with small GOS below 1°.

It is worth noting in Figure 11 that IPFs for the samples compressed at relatively low (973 K) or high (1273 K) temperatures exhibit somewhat increased pole density near <011>. Such

Figure 11. IPFs for the CA for the a–c) Fe–0.4C–18Mn and d–f) Fe–0.6C–18Mn steel samples subjected to hot compressions at a,d) $T = 973$ K and $\dot{\varepsilon} = 10^{-1}\,\text{s}^{-1}$, b,e) $T = 1173$ K and $\dot{\varepsilon} = 10^{-1}\,\text{s}^{-1}$, and c,f) $T = 1273$ K and $\dot{\varepsilon} = 10^{-3}\,\text{s}^{-1}$.
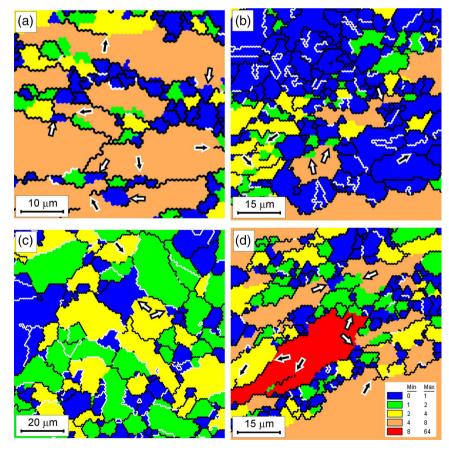
texture component is a common one for dislocation slip in fcc-metallic materials subjected to uniaxial compression.[43,44] Therefore, this texture component may result from continuous DRX mechanism, which contribution increases with a decrease in deformation temperature from hot to warm working,[37,45] as well as from the developed and then work-hardened DRX grains. The fraction of the latter ones increases with an increase in deformation temperature (see Figure 4). It should also be noted in Figure 11 that carbon content does not qualitatively affect the DRX texture, although the samples with lower carbon content exhibit stronger DRX texture because of faster DRX development.

3. Discussion

The deformation behavior during the studied compression tests suggests that the microstructural changes result from discontinuous DRX. Let us clarify the DRX nucleation and development. Selected portions of deformation microstructures in Figure 4 are represented in **Figure 12** in more detail. Numerous uncompleted grain boundaries with misorientations of $\theta \geq 15°$ are clearly seen in all the selected microstructural portions in Figure 12 as indicated by black arrows. The presence of such grain/subgrain boundaries is a distinctive feature of continuous DRX

mechanism, which is associated with progressive evolution of new grains in place of deformation subgrains owing to gradual increase in misorientations of deformation subboundaries up to typical values of ordinary high-angle grain boundaries during deformation.[23] The operation of continuous DRX has been frequently observed in low-to-medium SFE fcc alloys under conditions of warm working.[12,36–38] The rapid development of strain-induced high-angle boundaries in deformation micro-shear bands and close to original grain boundaries has been shown to result in a characteristic necklace microstructure.[46] Therefore, continuous DRX development could be expected in the present steels at 973 K (Figure 12a,d). The present results suggest, however, that continuous DRX develops concurrently with discontinuous one under all deformation conditions studied. Similar DRX behavior has been observed in duplex stainless steel during hot working.[13] The features of continuous DRX can be observed even in the DRX microstructure with a large fraction of grains with GOS below 1° (see black arrows in Figure 12b), although numerous annealing twins testify to negligibly small contribution of continuous DRX to overall microstructure evolution in this sample. Remarkable contributions of continuous DRX in the microstructure evolution should be expected at relatively low temperatures, e.g., 973 K. The grains evolved by continuous DRX are essentially the deformation subgrains experienced large rotations during deformation. Their orientations,

Figure 12. GOS in deformation microstructures of Fe–0.4C–18Mn steel samples subjected to compression at a) $T = 973$ K and $\dot{\varepsilon} = 10^{-2}$ s^{-1}, b) $T = 1073$ K and $\dot{\varepsilon} = 10^{-2}$ s^{-1}, and c) $T = 1173$ K and $\dot{\varepsilon} = 10^{-3}$ s^{-1}, and that in the Fe–0.6C–18Mn steel sample after compression at d) $T = 1073$ K and $\dot{\varepsilon} = 10^{-2}$ s^{-1}. High-angle grain boundaries and $\Sigma 3^n$ coincidence site lattice boundaries are indicated by the black and white lines, respectively.
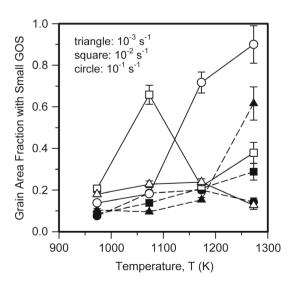
therefore, are associated with plastic flow, enhancing the deformation texture component, i.e., <011> along the CA in Figure 11a,d.

The white arrows in Figure 12 indicate the subgrains with small GOS below 1°. It should be noted that such subgrains locate near grain boundaries and, hence, partially bounded by both a portion of high-angle grain boundary and a low-angle dislocation subboundary. The high-angle boundaries may serve as recovery-assisted dislocation drains, leading to the evolution of small subgrains with relatively low dislocation density. Then, the local migration of the high-angle boundary portion toward work-hardened grain will result in new discontinuous DRX nucleus. This DRX grain nucleation promotes the evolution of necklace microstructures at an early stage of DRX (e.g., Figure 12a,d) or results in a new subsequent cycle of discontinuous DRX at its advanced stage on the steady-state deformation (see Figure 12b,c).

The rates of the nucleation and growth of DRX grains under conditions of multiple overlapping DRX cycles determine the mean DRX grain size and the relative fractions of DRX grains with different GOS. The effect of temperature and strain rate on the fraction of DRX grains with small GOS below 1° is represented in **Figure 13**. It is clearly seen that peaks against small GOS corresponding to rapid DRX development appear at definite temperature/strain rate conditions. A temperature of 973 K is not high enough for pronounced DRX development. Therefore, the fraction of grains with small GOS is small after deformation at this temperature in the both steels irrespective of strain rate in the range of 10^{-3}–$10^{-1}\,s^{-1}$. The rapid DRX development in the Fe–0.4C–18Mn steel samples during deformation at 1073 K results in large fraction of grains with small GOS at a strain rate of $10^{-2}\,s^{-1}$. Evidently, many DRX grains have a time to experience relatively large straining before the subsequent DRX cycle at a low strain rate, whereas the fraction of DRX grains itself is small during deformation at higher strain rate. As a result of DRX promotion with an increase in deformation temperature

to 1173–1273 K, the maximal fraction of the DRX grains with small GOS appears in the Fe–0.4C–18Mn steel samples at a high strain rate of $10^{-1}\,s^{-1}$. The steel with higher carbon content exhibits lower DRX kinetics. Thus, the maximal fraction of DRX grains with small GOS develops at the highest temperature of 1273 K and the lowest strain rate of $10^{-3}\,s^{-1}$ in the studied range of deformation conditions.

In contrast to statically recrystallized grains, the size of which has been discussed as a function of the density of recrystallizing nuclei in high-Mn steels because of site-saturated nucleation,[9,47,48] the present DRX grain size should depend on the grain growth rate, because the DRX nucleation occurs cyclically during deformation. In general, the rate of grain boundary migration depends directly on the boundary mobility (M) and the driving pressure (P).[49] The former depends on temperature and obeys an Arrhenius-type relationship ($M \approx \exp(-Q_M/RT$), where Q_M is an activation energy), whereas the latter can be related to the dislocation density (ρ) in the case of discontinuous recrystallization.[50,51] The dislocation density can be expressed by the flow stress (σ), using Taylor-type equation ($\sigma \approx \rho^{0.5}$).[52] In turn, the flow stress obeys a power law function of the temperature-compensated strain rate, $\sigma \approx Z^m$, where m of about 0.17 is obtained for the present steels compressed under hot-working conditions (Figure 3). Therefore, the driving pressure can be related to the deformation conditions.

$$P \approx \dot{\varepsilon}^{2m}\exp\frac{2mQ}{RT} \qquad (4)$$

The same σ–Z dependence for the both steels in Figure 3 suggests the same driving pressure for the DRX grain growth irrespective of some difference in the carbon content in the present steels. Then, the time (t) dependence for the size of the growing DRX grains can be expressed as follows.

$$D \approx tMP \approx t\dot{\varepsilon}^{2m}\exp\frac{2mQ - Q_M}{RT} \qquad (5)$$

The temperature dependences of the DRX grain size evolved in the present steel samples under various strain rates are shown in **Figure 14**. The DRX grain size in Figure 14 follows Equation (5) in the range of hot working at 1073–1273 K with a slope of ($2mQ - Q_M$) of −84 and −73 kJ mol^{-1} for the Fe–0.4C–18Mn and Fe–0.6C–18Mn steel samples, respectively. Using $Q = 263\,kJ\,mol^{-1}$ from Figure 2, the activation energy for grain boundary mobility can be calculated as 173 and 162 kJ mol^{-1} for the steels with a carbon content of 0.4% and 0.6%, respectively. These values of Q_M are quite close to that of a grain boundary diffusion of 167 kJ mol$^{-1[27]}$ that validates the speculation mentioned earlier. Small difference in the grain boundary mobility is associated with a redistribution of carbon atoms in the moving grain boundary and responsible to the finer DRX grain size in the steel samples with larger carbon content (Figure 10), whereas the flow stresses are entirely determined by the deformation conditions irrespective of carbon content in the range of 0.4–0.6% (Figure 3). Similar effect of solutes on the deformation behavior and DRX has been observed in copper samples with different purities.[53] In contrast to this study, however, the different effects of impurities on the flow stress and DRX grain size have been revealed in high purity coppers.

Figure 13. Effect of deformation temperature and strain rate on the area fraction with small GOS below 1° in DRX microstructures evolved in Fe–0.4C–18Mn (open symbols) and Fe–0.6C–18Mn (filled symbols) steel samples subjected to hot compression.
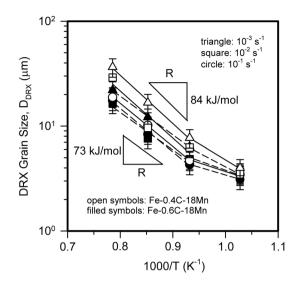
Figure 14. Effect of deformation temperature on the DRX grain size in Fe–0.4C–18Mn and Fe–0.6C–18Mn steel samples subjected to hot compression.

Namely, the DRX grain size has increased with an increase in purity, whereas the flow stress has been almost independent of an impurity content below 1 ppm. The disappearance of the impurity effect on the flow stress during hot deformation of copper with only high purities can be associated with properties of impurities, which are mainly substitution solutes. In contrast, the present steels are differentiated with content of carbon, which is interstitial solute. The effect of interstitials on the flow stress during hot working seems to be much weaker as compared with substitution solutes. Thus, remarkable difference in the effect of alloying extent on the flow stress and the DRX grain size is observed in the present steels with varying the carbon content from 0.4% to 0.6%.

4. Conclusions

The deformation behavior and microstructure evolution were studied in high-Mn TWIP steels with different carbon contents, i.e., Fe–0.4C–18Mn and Fe–0.6C–18Mn, by means of hot isothermal compression tests at the temperatures of 973–1373 K and the strain rates of 10^{-3}–10^{-1} s^{-1}. The main results can be summarized as follows.

1) The deformation behavior was characterized by the development of discontinuous DRX, which was promoted by an increase in deformation temperature and/or a decrease in strain rate, resulting in specific increase in the flow stress to its maximum at early deformation followed by strain softening during further deformation. The peak flow stress obeyed a power law relationship with the temperature-compensated strain rate with an exponent of 0.17 in the both steels irrespective of different carbon contents. On the other hand, a decrease in the carbon content advanced the DRX development. The same fractions in the range of 0.3–0.8 of the grains with GOS below 4° can be obtained in the Fe–0.4C–18Mn steel after straining to $\varepsilon = 1$ at temperatures about 50–100 K below those for the Fe–0.6C–18Mn steel. 2) Variations in the DRX kinetics with deformation conditions resulted in the specific distributions of the grain boundary misorientations and GOS among the DRX grains. The large area fraction above 0.6 of DRX grains with small GOS below 1° corresponding to rapid DRX development appeared at definite temperature/strain rate conditions along with a large ratio above 1 of high-angle (around 60°) boundary fraction to low-angle (below 4°) subboundary fraction. 3) The DRX development could be evaluated by the area fraction of grains with GOS below 4°. The texture of DRX grains was also determined by the orientations of grains with GOS below 4° irrespective of any differences in the kinetics of individual DRX cycle, which can be roughly related to the faction of DRX with small GOS below 1°. 4) The DRX grain size in the both steels could be expressed by a power law function of the temperature-compensated strain rate with an exponent of −0.25, although larger DRX grains were evolved in the steel with lower carbon content. The grain boundary mobility for the DRX grain growth was characterized by the activation energies of 173 and 162 kJ mol^{-1} for the Fe–0.4C–18Mn and Fe–0.6C–18Mn steels, respectively, which are close to that for grain boundary diffusion.

5. Experimental Section

Two high-Mn steels, Fe–0.44C–17.4Mn and Fe–0.62C–18.0Mn (all in weight percent), hereafter Fe–0.4C–18Mn and Fe–0.6C–18Mn, respectively, were examined. The steel ingots were produced by an induction melting and then subjected to hot rolling at 1423 K with 60% reduction. The initial microstructures of Fe–0.4C–18Mn and Fe–0.6C–18Mn steels consisted of equiaxed grains with the average grain sizes of 48 and 32 μm, respectively. A series of isothermal compression tests to a strain of 1.0 was performed at the strain rates of 10^{-1}–10^{-3} s^{-1} at the temperatures of 973–1373 K using an INSTRON 300LX testing machine on prismatic specimens with a dimension of 10 mm × 10 mm × 15 mm with boron nitride powders as a lubricant. Relatively low strain rates were used to slow down kinetics of possible post-DRX.[54] Just after the compression was ceased, the specimens were rapidly cooled by in situ water jet to diminish an effect of post-DRX on the developed microstructures. The structural observations were carried out at the center portion of the compressed specimens using a Nowa NanoSem 450 field emission gun scanning electron microscope (SEM) operated at 30 kV and equipped with an electron back scattering diffraction (EBSD) pattern analyzer incorporating an orientation imaging microscopy (OIM) system with TexSEM Laboratories OIM Analysis 6 software. The areas of 400 μm × 400 μm were scanned with a step size of 1 μm to obtain OIM images for each compressed sample. The OIM images with an average confidence index of 0.3–0.6 depending on the specimen processing conditions were subjected to clean up procedures setting a minimal confidence index of 0.1. The GOS was mapped setting the grain tolerance angle of 5°. The mean grain size was measured using the linear intercept method on the OIM images, averaging the distance between high-angle boundaries, i.e., those with misorientations of $\theta \geq 15°$, along and crosswise the CA.

Conflict of Interest

The authors declare no conflict of interest.

Keywords

[1] L. W. Cheah, *PhD Thesis*, Massachusetts Institute of Technology **2010**.
[2] M. Y. Demeri, *Advanced High-Strength Steels: Science, Technology, and Applications*, ASM International, Materials Park, Ohio **2013**.
[3] J. Rowe, *Advanced Materials in Automotive Engineering*, Woodhead Publishing Limited, Cambridge **2012**.
[4] Y. S. Jin, *Metall. Ital.* **2011**, *103*, 43.
[5] P. Kusakin, A. Belyakov, C. Haase, R. Kaibyshev, D. A. Molodov, *Mater. Sci. Eng. A* **2014**, *617*, 52.
[6] B. C. De Cooman, Y. Estrin, S. K. Kim, *Acta Mater.* **2018**, *142*, 283.
[7] R. Ueji, N. Tsuchida, D. Terada, N. Tsuji, Y. Tanaka, A. Takemura, K. Kunishige, *Scr. Mater.* **2008**, *59*, 963.
[8] V. Torganchuk, A. Belyakov, R. Kaibyshev, *Mater. Sci. Eng. A* **2017**, *708*, 110.
[9] Z. Yanushkevich, A. Belyakov, R. Kaibyshev, C. Haase, D. A. Molodov, *Mater. Charact.* **2016**, *112*, 180.
[10] P. Kusakin, A. Belyakov, D. A. Molodov, R. Kaibyshev, *Mater. Sci. Eng. A* **2017**, *687*, 82.
[11] H.-W. Yen, M. Huang, C. P. Scott, J.-R. Yang, *Scr. Mater.* **2012**, *66*, 1018.
[12] Z. Yanushkevich, A. Belyakov, R. Kaibyshev, *Acta Mater.* **2015**, *82*, 244.
[13] P. Cizek, *Acta Mater.* **2016**, *106*, 129.
[14] T. Sakai, J. J. Jonas, *Acta Metall.* **1984**, *32*, 189.
[15] J. J. Jonas, X. Quelennec, L. Jiang, É. Martin, *Acta Mater.* **2009**, *57*, 2748.
[16] D. Li, Y. Feng, Z. Yin, F. Shangguan, K. Wang, Q. Liu, F. Hu, *Mater. Sci. Eng. A* **2011**, *528*, 8084.
[17] P. Dolzhenko, M. Tikhonova, R. Kaibyshev, A. Belyakov, *Metals* **2019**, *9*, 30.
[18] A. Belyakov, R. Kaibyshev, V. Torganchuk, *Steel Res. Int.* **2017**, *88*, 1600123.
[19] M. Ghasri-Khouzani, J. R. McDermid, *Mater. Sci. Eng. A* **2015**, *621*, 118.
[20] O. Bouaziz, S. Allain, C. P. Scott, P. Cugy, D. Barbier, *Curr. Opin. Solid State Mater. Sci.* **2011**, *15*, 141.
[21] L. Chen, H.-S. Kim, S.-K. Kim, B. C. De Cooman, *ISIJ Int.* **2007**, *47*, 1804.
[22] X.-M. Chen, Y. C. Lin, D.-X. Wen, J.-L. Zhang, M. He, *Mater. Des.* **2014**, *57*, 568.
[23] T. Sakai, A. Belyakov, R. Kaibyshev, H. Miura, J. J. Jonas, *Prog. Mater. Sci.* **2014**, *60*, 130.
[24] K. Huang, R. E. Logé, *Mater. Des.* **2016**, *111*, 548.
[25] C. Zener, J. H. Hollomon, *J. Appl. Phys.* **1944**, *15*, 22.
[26] M.-S. Chen, Y. C. Lin, X.-S. Ma, *Mater. Sci. Eng. A* **2012**, *556*, 260.
[27] H. J. Frost, M. F. Ashby, *Deformation Mechanism Maps: The Plasticity and Creep of Metals and Ceramics*, Pergamon Press, Oxford, UK **1982**.
[28] H. J. McQueen, N. D. Ryan, *Mater. Sci. Eng. A* **2002**, *322*, 43.
[29] M. El Wahabi, J. M. Cabrera, J. M. Prado, *Mater. Sci. Eng. A* **2003**, *343*, 116.
[30] M. Tikhonova, R. Kaibyshev, A. Belyakov, *Adv. Eng. Mater.* **2018**, *20*, 1700960.
[31] T. Sakai, J. J. Jonas, in *Encyclopedia of Materials: Science Technology*, Elsevier, Oxford **2001**, pp. 7079–7084.
[32] T. Sakai, M. Ohashi, *Mater. Sci. Technol.* **1990**, *6*, 1251.
[33] K. Graetz, C. Miessen, G. Gottstein, *Acta Mater.* **2014**, *67*, 58.
[34] D. Ponge, G. Gottstein, *Acta Mater.* **1998**, *46*, 69.
[35] A. Guria, G. K. Mandal, P. Hodgson, J. H. Beynon, S. G. Chowdhury, *Metall. Mater. Trans. A* **2015**, *46*, 4423.
[36] A. Belyakov, T. Sakai, H. Miura, R. Kaibyshev, *ISIJ Int.* **1999**, *39*, 592.
[37] M. Tikhonova, A. Belyakov, R. Kaibyshev, *Mater. Sci. Eng. A* **2013**, *564*, 413.
[38] M. Tikhonova, V. Torganchuk, F. Brasche, D. A. Molodov, A. Belyakov, R. Kaibyshev, *Metall. Mater. Trans. A* **2019**, *50*, 4245.
[39] T. Maki, K. Akasaka, K. Okuno, I. Tamura, *Trans. Iron Steel Inst. Jpn.* **1982**, *22*, 253.
[40] W. B. Hutchinson, E. Nes, in *Grain Growth Polycrystalline Materials*, Trans Tech Publications Ltd, Rome **1992**.
[41] O. Engler, H. E. Vatne, E. Nes, *Mater. Sci. Eng. A* **1996**, *205*, 187.
[42] M. Frommert, G. Gottstein, *Mater. Sci. Eng. A* **2009**, *506*, 101.
[43] J. F. W. Bishop, *J. Mech. Phys. Solids* **1955**, *3*, 130.
[44] J. Gil Sevillano, P. van Houtte, E. Aernoudt, *Prog. Mater. Sci.* **1980**, *25*, 69.
[45] P. Dolzhenko, M. Tikhonova, T. Sakai, A. Belyakov, R. Kaibyshev, *Mater. Perform. Charact.* **2019**, *8*, 808.
[46] N. Dudova, A. Belyakov, T. Sakai, R. Kaibyshev, *Acta Mater.* **2010**, *58*, 3624.
[47] L. Bracke, K. Verbeken, L. Kestens, J. Penning, *Acta Mater.* **2009**, *57*, 1512.
[48] C. Haase, M. Kühbach, L. A. Barrales-Mora, S. L. Wong, F. Roters, D. A. Molodov, G. Gottstein, *Acta Mater.* **2015**, *100*, 155.
[49] F. J. Humphreys, M. Hatherly, *Recrystallization and Related Annealing Phenomena*, 2nd ed., Elsevier Ltd, Amsterdam/New York **2004**.
[50] E. I. Poliak, J. J. Jonas, *Acta Mater.* **1996**, *44*, 127.
[51] Y.-X. Liu, Y. C. Lin, H.-B. Li, D.-X. Wen, X.-M. Chen, M.-S. Chen, *Mater. Sci. Eng. A* **2015**, *626*, 432.
[52] X. Quelennec, N. Bozzolo, J. J. Jonas, R. Loge, *ISIJ Int.* **2011**, *51*, 945.
[53] W. Gao, A. Belyakov, H. Miura, T. Sakai, *Mater. Sci. Eng. A* **1999**, *265*, 233.
[54] J. Liu, Y. G. Liu, H. Lin, M. Q. Li, *Mater. Sci. Eng. A* **2013**, *565*, 126.